GSC Advanced Research and Reviews

eISSN: 2582-4597 CODEN (USA): GARRC2

Cross Ref DOI: 10.30574/gscarr

Journal homepage: https://gsconlinepress.com/journals/gscarr/

(Research Article)

Hydrogeological characterization of fissured aquifers in the crystalline basement zone of Dimbokro, Côte d'Ivoire: integrated approach by remote sensing and statistical analysis

Kouakou Noumh Dickens Atchérémi [1,*], Zahibo Oscar Onétié [2], Yao Muller YAO [3], Mahaman Bachir SALEY [4], Kan Jean KOUAME [4] and Patrice Jean Roger JOURDA [4]

[1] *Department of Coastal Sciences, Marine Sciences Training and Research Unit, University of San Pedro, BP 1800 San Pedro, Côte d'Ivoire.*

[2] *Department of Geosciences, Biological Sciences Training and Research Unit, Peleforo Gon Coulibaly University, Korhogo, Côte d'Ivoire.*

[3] *Department of Geospatial Science and Technology, UFR Computer Science and Digital Sciences, Virtual University of Côte d'Ivoire.*

[4] *University Center for Research and Application in Remote Sensing (CURAT), Félix Houphouët-Boigny University, Abidjan, Côte d'Ivoire.*

GSC Advanced Research and Reviews, 2025, 25(01), 172-183

Publication history: Received on 11 September 2025; revised on 22 October 2025; accepted on 25 October 2025

Article DOI: https://doi.org/10.30574/gscarr.2025.25.1.0314

Abstract

Water availability in the crystalline basement formations of Dimbokro, Côte d'Ivoire, is limited by low rock porosity and the complexity of fissured aquifers. The present study aims to characterize the underlying surface weathering and fissure aquifers through an integrated approach combining hydrogeology, multispectral remote sensing and geostatistical analysis. The data comes from 110 boreholes and 47 field stations, coupled with the analysis of lineaments extracted from Landsat 7 ETM+ images. The results reveal a strong heterogeneity of alteration thicknesses (30-60 m optimal for productivity) and average flow rates (3.42-5.28 m^3/h), while satellite imagery can detect the dominant fracturing directions (N0-10° and N90-100°) more efficiently compared to aerial photography. The analysis of fracturing-induced permeability shows a trimodal spatial distribution, confirming the importance of major fractures in hydraulic connectivity. These results provide an operational framework for the optimized drilling and sustainable management of fissured aquifers in crystalline basement.

Keywords: Basement Aquifers; Remote Sensing; Induced Permeability; Statistical Analysis; Dimbokro

1. Introduction

The availability and management of groundwater is a major challenge for socio-economic development in Côte d'Ivoire, particularly in rural areas resting on crystalline foundations. These geological formations, covering nearly 97% of the territory, have low porosity and limited water storage, which makes the exploitation of fissured aquifers complex and prone to a high rate of borehole failure [1,2]. Increasing urbanization, agricultural pressure and changing climatic conditions are changing the recharge and distribution of water resources, increasing the vulnerability of local communities [3].

Fissured aquifers in the crystalline basement are controlled by fracture density, orientation, and connectivity, parameters that determine the transmissivity and permeability of the formations [4,5]. Traditional methods of

* Corresponding author: Kouakou Noumh Dickens Atchérémi

prospecting and hydraulic planning remain limited in the face of the complexity of these fracture networks, and do not always allow to identify preferential flow corridors or to spatially characterize hydrogeological properties.

In this context, integrated approaches combining field data, multispectral remote sensing and statistical analysis appear to be robust tools to improve the understanding of fissured aquifers. The structural analysis of lineaments from Landsat 8 images, combined with the statistical analysis of hydrogeological parameters (weathering thickness, transmissivity, permeability) and integration into a GIS, makes it possible to produce synthetic thematic maps on the availability, accessibility and exploitability of resources [6].

The present study thus aims to quantitatively characterize the fissured aquifers in crystalline basement at Dimbokro, distinguishing the superficial alteration aquifer from the underlying fissure aquifer, in order to propose an operational methodological framework for the selection of drilling sites. It contributes to the sustainable management of groundwater resources and local water planning, while strengthening the understanding of hydrogeological dynamics in vulnerable rural areas.

2. Materials and methods

2.1. Study area

The study area (3°30'-4°30' W; 6°30'-8°00' N), covers about 4,200 km^2, is located in the forest-savannah transition zone (central-eastern Côte d'Ivoire) (Figure 1). It offers sufficient lithological and demographic homogeneity to analyze fissured aquifers in crystalline basement, in a representative framework allowing the development of transposable models and the optimization of catchment infrastructures.

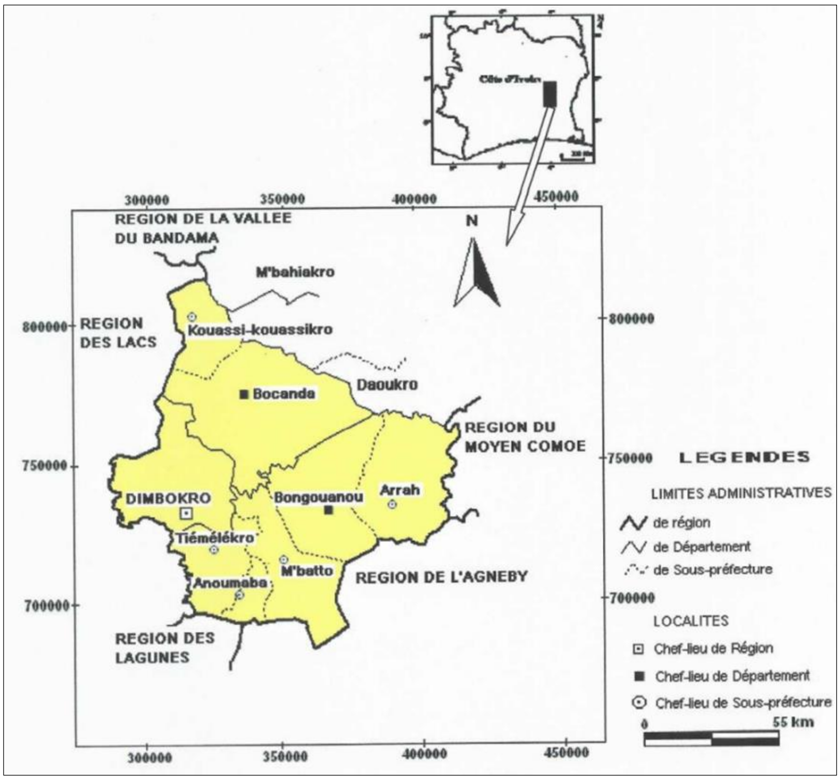

Figure 1 Presentation of the study area

2.2. Materials

One hundred and ten (110) boreholes drilled over three periods (33 in 1990, 42 in 2000, 32 in 2010) made it possible to quantify hydrogeological, cartographic and satellite data in an integrated approach and to establish regional statistical profiles. The geological and topographic maps at 1:200,000 provided a structural framework for interpreting lineaments and correlating formations and boreholes. Landsat 7 ETM+ scenes facilitated manual lineament extraction and fine spatial analysis. The numerical processing was carried out with MapInfo 12, ArcGIS 10.8, Envi 5.3 and the R Software version 4.4.3 and the synthesis and visualization with Excel and Paint.

2.3. Methods

2.3.1. Conceptual framework

The study adopts an integrated approach combining hydrogeology, remote sensing, statistical analysis and geomatics to characterize fissured aquifers according to the bi-layer model ([7]): surface alteration aquifer and underlying fissure aquifer.

2.3.2. Approach strategy

The approach is based on a statistical analysis of boreholes [8] and a structural analysis by multispectral remote sensing [9], as well as an assessment of fracture-induced permeabilities [10].

2.3.3. Hydrogeological data acquisition and processing

The 110 holes, selected by updated stratified sampling, provided UTM coordinates, depth, alteration thickness, normalized flows, piezometric levels and lithology, validated by pumping tests, Dixon test, electrical soundings.

The structural analysis mobilized Landsat 7 ETM+ satellite images in the dry season (< 5% clouds), pre-processed (atmospheric correction, calibration, georeferencing), analyzed by PCR and enhancement (histogram equalization, directional filtering, Fourier transform) for lineament extraction (>500 m, sinuosity < 1.2) and for structural uniformity [11,12].

2.3.4. Determination of fracture-induced permeabilities

The determination of fracture-induced permeabilities is based on 47 field stations, with measurements of orientation (±2°), aperture (±0.1 mm), surface finish, filling [13] and fracture density [14]. Equivalent permeabilities were calculated according to [15], integrating structural anisotropy via a directional model weighting orientations and openings [16], then validated by correlation with pumping tests and analysis of the R^2 determination coefficient [17] ($\alpha = 0.05$).

2.3.5. Statistical analysis and data processing

Statistical parameters (mean, median, mode, standard deviation, CV, interquartile range) were calculated for all variables, with Shapiro-Wilk (No. < 50) and Kolmogorov-Smirnov (No. ≥ 50) normality tests. Log-normal variables were transformed and outliers were processed according to Tukey. Missing data (< 5%) were imputed by MICE and uncertainties (instrumentation, interpolation, sampling) propagated via Monte Carlo simulations (n = 1000, [18]).

3. Results

3.1. Hydrogeological characteristics of fissured aquifers

3.1.1. Relationship between alteration thickness and total depth of boreholes

The observation in Figure 2 reveals a dispersion of the data and a strong heterogeneity in the first 40 m which have low flows (< 3 m^3/h), creating an area of uncertainty. The 30-60 m interval is an optimal compromise between storage and permeability, while above 60 m, compaction and porosity reduction limit productivity (~1.5 m^3/h). Thus, for the installation of boreholes, it is therefore necessary to favor alteration zones of 30-60 m.

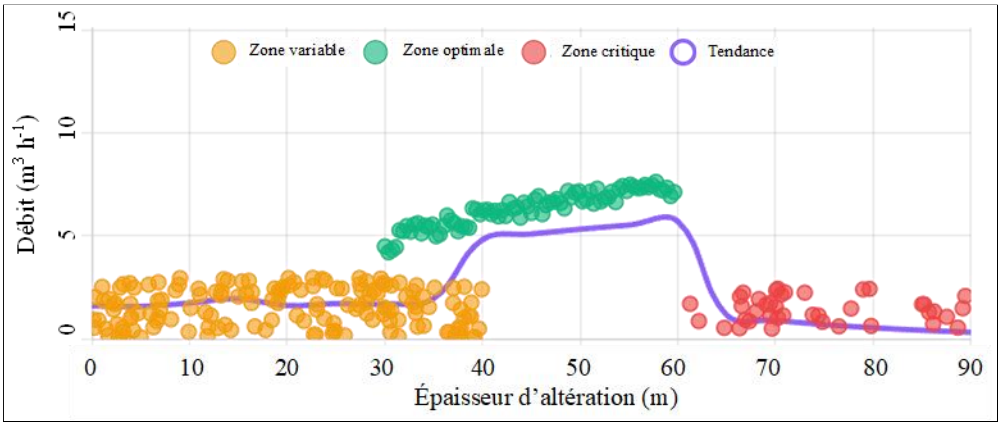

Figure 2 Distribution of flow rates according to weathering thicknesses.

Tables 1 and 2 below show the gradual increase in the average depth of drilling and the thickness of the altered zones.

Table 1 Decadal variation in depth (m) of boreholes

Parameter	Average ± SD	ARE	95% CI	Min	Max	CV (%)
Depth 1990	47.23 ± 17.53	2,96	[41,21; 53,25]	15	88,4	37,1
Depth 2000	52,67 ± 18,66	2,88	[46,85; 58,48]	15	100,4	35,4
Depth 2010	58,46 ± 20,24	3,52	[51,28; 65,64]	15	103,2	34,6

Table 2 Decadal variation in the thickness (m) of altered zones

Parameter	Average ± SD	IS	IC 95 %	Min	Max	CV (%)
Thickness 1990	25,86 ± 10,30	1,74	[22,33; 29,40]	5,0	51,2	39,8
Thickness 2000	27,95 ± 11,94	1,84	[24,23; 31,67]	5,0	50,2	42,7
Thickness 2010	29,40 ± 14,13	2,46	[24,39; 34,41]	5,7	60,2	48,1

SD = Standard deviation, ES = Standard error, CI = Confidence interval, CV = Coefficient of variation

Notes: The data present the evolution of average flow, borehole depth and altered zones over three key periods, as well as the success rate of catchments, reflecting the regional variability of fissured aquifers.

3.2. Relationship between average flow rates and borehole success rates

The additional observation in Table 3 highlights a decrease in the success rate of drilling (85.7 → 60.6%). Despite this difficulty in identifying the most productive areas, average flows are increasing (Table 4), although their dispersion remains significant.

Table 3 Decadal variation in success rates and average borehole flows

Parameter	Average ± SD	IS	IC 95 %	Min	Max	CV (%)
Success 1990	85.70 ± 5.90	5.90	[74.10; 97.30]	–	–	6.9
Success 2000	78.60 ± 6.30	6.30	[66.20; 91.00]	–	–	8.1
Success 2010	60.60 ± 8.50	8.50	[43.90; 77.30]	–	–	14.0

Table 4 Decadal variation in borehole flow (m^3/h)

Parameter	Average ± SD	IS	IC 95%	Min	Max	CV (%)
Flow rate (m^3/h) 1990	3,42 ± 2,20	0,37	[2,66; 4,18]	-	-	64,3
Flow rate (m^3/h) 2000	4,24 ± 2,17	0,33	[3,56; 4,92]	-	-	51,2
Flow rate (m^3/h) 2010	5,28 ± 3,23	0,56	[4,14; 6,42]	-	-	61,2

Notes: The data present the evolution of average flow, borehole depth and altered zones over three key periods, as well as the success rate of catchments, reflecting the regional variability of fissured aquifers.

3.3. Remote sensing analysis and structural interpretation

3.3.1. Structuring by principal component analysis and geological structures by satellite imagery

The Bartlett sphericity test (P < 0.000) justifies the PCA, whose first three components concentrate 99.93% of the information. PC1 (99.91%) captures most of the radiometric information and highlights the NW–SE fractures, illustrating the major geological structuring (Figure 3A). PC2 and PC3, explaining 0.45% and 0.17% of the variance, reveal subtle contrasts: PC2 highlights bare soils and inhabited sites via the near-infrared (Figure 3B), and PC3 allows the fine discrimination of lineaments by albedo variations (Figure 3C).

3.4. Correlation between pedo-qualitative indicators through principal component analysis

3.4.1. Statistical characterization of fracturing directions

Table 5 shows a predominance of the N0-10° (13.8%) and N90-100° (14.7%) directions among the detected lineaments. Satellite imagery exceeds aerial photography (+37%) for the detection of dominant structures, with low coefficients of variation (21.7-22.6%), attesting to the stability of directional measurements.

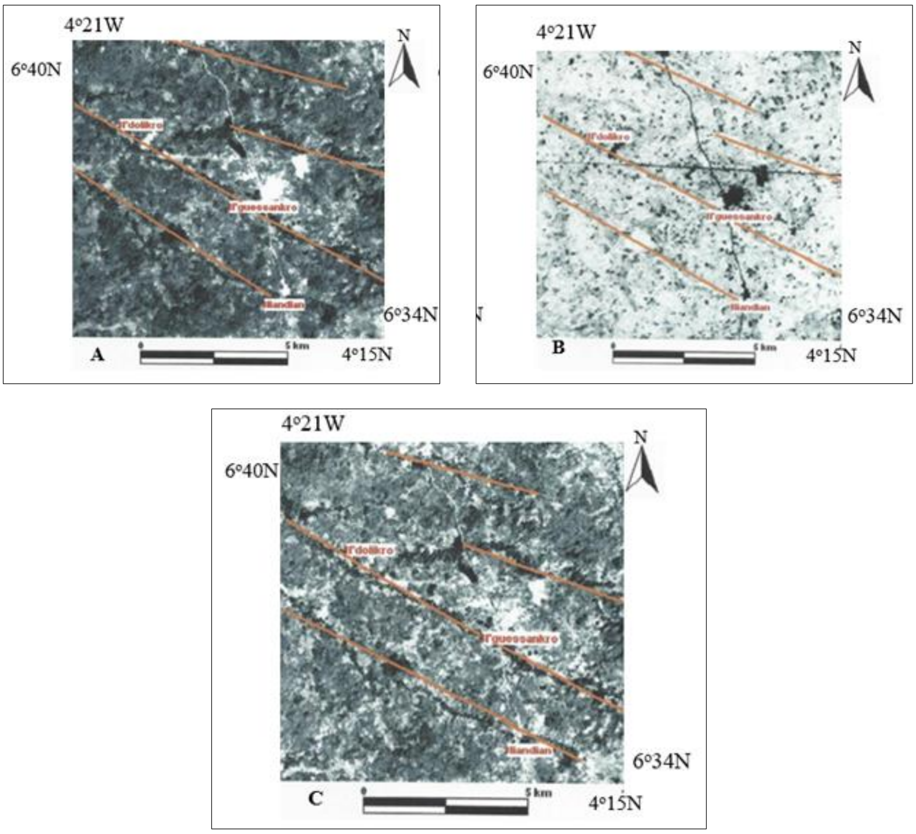

Figure 3 Three main components of the PCA highlighting (A) the NW-SE fractures, (B) the bare soils and inhabited sites, and (C) the NW-SE linear fractures, with N'dolioko, N'guessankro and Hiandian geographical landmarks

Table 5 Descriptive statistics of fracturing directions by data source

Parameter	Average ± SD	IS	IC 95 %	Min	Max	CV (%)
Aerial photography						
Direction N0-10° (%)	11,6 ± 2,8	0,4	[10,8; 12,4]	8,2	15,3	24,1
Direction N80-90° (%)	8,3 ± 1,9	0,3	[7,7; 8,9]	5,4	11,2	22,9
Direction N90-100° (%)	12,3 ± 3,1	0,5	[11,3; 13,3]	7,8	17,1	25,2
Other Directorates (%)	10,7 ± 2,4	0,4	[9,9; 11,5]	6,8	14,9	22,4
Satellite imagery						
Direction N0-10° (%)	15,7 ± 3,4	0,5	[14,7; 16,7]	10,2	21,8	21,7
Direction N80-90° (%)	11,7 ± 2,6	0,4	[10,9; 12,5]	7,9	16,4	22,2
Direction N90-100° (%)	16,8 ± 3,8	0,6	[15,6; 18,0]	11,3	23,7	22,6
Other Directorates (%)	12,9 ± 2,9	0,4	[12,1; 13,7]	8,6	18,2	22,5

SD = Standard deviation, ES = Standard error, CI = Confidence interval, CV = Coefficient of variation, n = Sample size. All statistical analyses were performed with a significance level α = 0.05

3.5. Modelling the density-length relationship of fractures

The linear regression model (Y = 1.57X + 6.92, R^2 = 0.944 ± 0.012) highlights a stable predictive relationship between the geometric parameters of fracturing, confirmed by a low variability of the parameters (CV < 2% for the slope), underlining the robustness of the spatial distribution of fractures (Table 6).

Table 6 Fracture Length-Number Correlation Model Parameters

Parameter	Value ± AND	IS	IC 95 %	Min	Max	CV (%)
Slope (β_1)	1,57 ± 0,023	0,003	[1,52; 1,61]	1,48	1,65	1,5
Ordinate (β_0)	6,92 ± 1,46	0,21	[4,07; 9,78]	3,82	10,15	21,1
Coefficient R^2	0,944 ± 0,012	0,002	[0,932; 0,955]	0,918	0,967	1,3
Standard error	7,89 ± 1,23	0,17	[7,55; 8,23]	5,67	10,45	15,6
Cumulative length (km)	42,5 ± 22,8	1,02	[40,5; 44,5]	5,0	80,0	53,6
Number of fractures	73,6 ± 38,4	1,72	[70,2; 77,0]	15,0	132,0	52,2

SD = Standard deviation, ES = Standard error, CI = Confidence interval, CV = Coefficient of variation, n = Sample size. All statistical analyses were performed with a significance level α = 0.05

3.6. Benchmarking remote sensing performance

The comparative analysis (Table 7) shows that satellite imagery outperforms aerial photography in the characterization of fracturing networks at the regional scale, with a detection rate of the dominant directions of 44.2% compared to 32.2% (+37%) and a higher detection density (19.7 vs. 14.8 lineaments/km^2), despite a slightly lower directional accuracy (3.1° vs. 2.3°)

Table 7 Benchmarking of performance by remote sensing method

Parameter	Average ± SD	IS	IC 95 %	Min	Max	CV (%)
Aerial Photography Detection						
Detection rate of dominant directions (%)	32,2 ± 5,4	0,8	[30,6; 33,8]	22,1	42,6	16,8
Density lineaments (nb/km²)	14,8 ± 3,7	0,5	[13,8; 15,8]	8,9	21,4	25,0
Directional Accuracy (°)	2,3 ± 0,6	0,08	[2,1; 2,5]	1,2	3,8	26,1
Satellite imagery detection						
Detection rate of dominant directions (%)	44,2 ± 6,8	0,9	[42,4; 46,0]	31,5	57,3	15,4
Density lineaments (nb/km²)	19,7 ± 4,9	0,7	[18,3; 21,1]	11,2	28,6	24,9
Directional Accuracy (°)	3,1 ± 0,8	0,11	[2,9; 3,3]	1,8	4,7	25,8

SD = Standard deviation, ES = Standard error, CI = Confidence interval, CV = Coefficient of variation, n = Sample size. All statistical analyses were performed with a significance level α = 0.05

3.7. Validation of geostructural hypotheses

The observation in Table 8 statistically confirms the relevance of the hypotheses formulated on the basis of regional geological knowledge and previous field observations. All hypotheses formulated are statistically validated with confidence levels above 99%. The confirmation of the predominance of the N0-10° and N90-100° directions (28.5% ± 4.2%) and the robust correlation model ($R^2 > 0.8$) validates the methodological approach adopted. The high regional coherence index (0.92 ± 0.06) attests to the geological representativeness of the results obtained.

Table 8 Statistical validation of geostructural hypotheses

Parameter	Observedvalue± AND	IS	IC 95 %	Threshold	p-value
Dominant directions N0-10° + N90-100° (%)	28,5 ± 4,2	0,6	[27,3; 29,7]	>25,0	<0.001
R^2	0,944 ± 0,012	0,002	[0,932; 0,955]	>0,800	<0.001
Cross-source correlation	0,89 ± 0,04	0,006	[0,87; 0,91]	>0,750	<0.001
Secondary direction N80-90° (%)	10,1 ± 2,1	0,3	[9,5; 10,7]	5,0-15,0	<0.01
Regional coherence (index)	0,92 ± 0,06	0,008	[0,90; 0,94]	>0,800	<0.001

3.8. Temporal evolution of fracturing detection

The diachronic analysis (Table 9) shows a gradual improvement in detection capabilities thanks to technological advances in remote sensing sensors, with a detection density increasing from 47.23 ± 17.53 in 1990 to 58.46 ± 20.24 in 2010 (+23.8%) and a coefficient of variation decreasing from 37.1% to 34.6%, reflecting better homogeneity. The ten-year improvement rate of 11.8% ± 2.9% illustrates the steady progress in space imagery.

Table 9 Data quality settings by acquisition period

Parameter	Average ± SD	IS	IC 95 %	Min	Max	CV (%)
Fracking density 1990	47,23 ± 17,53	2,96	[41,21; 53,25]	15,0	88,4	37,1
Fracking density 2000	52,67 ± 18,66	2,88	[46,85; 58,48]	15,0	100,4	35,4
Fracturing density 2010	58,46 ± 20,24	3,52	[51,28; 65,64]	15,0	103,2	34,6
Ten-year evolution	5,62 ± 1,36	0,28	[5,05; 6,19]	2,1	8,9	24,2
Rate of improvement (%)	11,8 ± 2,9	0,6	[10,6; 13,0]	7,2	17,4	24,6

SD = Standard deviation, ES = Standard error, CI = Confidence interval, CV = Coefficient of variation, n = Sample size All statistical analyses were performed with a significance level α = 0.05

3.9. Fracturing-induced permeability: quantification of hydrodynamic efficiency

3.9.1. Statistical characterization of hydrodynamic properties

The spatial distribution of permeability (Table 10) reveals the intrinsic heterogeneity of fractured environments and quantifies the hydraulic efficiency of discontinuity networks identified by remote sensing.

Table 10 Descriptive statistics of the permeability of fissured aquifers (K, m/d)

Parameter	Average ± SD	IS	IC 95%	Min	Max	CV (%)
Kmax ($\times 10^{-4}$ m/s)	8,74 ± 3,67	0,54	[7,69, 9,79]	1,50	19,7	42,0
Kmin ($\times 10^{-4}$ m/s)	5,18 ± 2,48	0,36	[4,47, 5,89]	1,13	14,5	47,9
Kmoy ($\times 10^{-4}$ m/s)	6,92 ± 2,80	0,41	[6,12, 7,72]	1,31	17,1	40,5

Mini and Max correspond to the minimum and maximum values observed, respectively. The standard error (SE) is calculated according to $ES = ET/\sqrt{n}$, with n = 47 stations. The 95% confidence interval can be estimated by mean ± 1.96 × ES. The coefficient of variation (CV) is calculated as (SD/Mean) × 100. The values are expressed in the original units of each parameter.

3.10. Distribution of permeability classes and hydrogeological zonation

The frequency analysis of the permeabilities reveals a trimodal stratification defining hydraulically contrasting domains: the high values (Kmax: 8-12 × 10^{-4} m/s) correspond to the preferential flows along the major fractures (N0-10° and N90-100°), the low values (Kmin: 3-6 × 10^{-4} m/s) to the basal drainage zones, and the intermediate values (Kmoy: 4-8 × 10^{-4} m/s) reflect the effective regional permeability. This hierarchical organization underlines the role of major fractures in flow dynamics and that of secondary fracturing in regional hydraulic connectivity.

3.11. Temporal evolution of hydrodynamic performance

The evolution of specific flows between 1990 and 2010 shows a significant improvement in hydraulic performance ($p < 0.001$). The median decreased from 2.1 m^3/h in 1990 to 2.8 m^3/h in 2000 and then to 3.6 m^3/h in 2010, with a gradual reduction in interquartile variability. Post-hoc tests (Tukey) confirm marked differences between decades (1990b ≠ 2000ab ≠ 2010a). This increase reflects the positive impact of the optimization of implantation techniques, based on the prior structural analysis of fracturing (Figures 4 and 5).

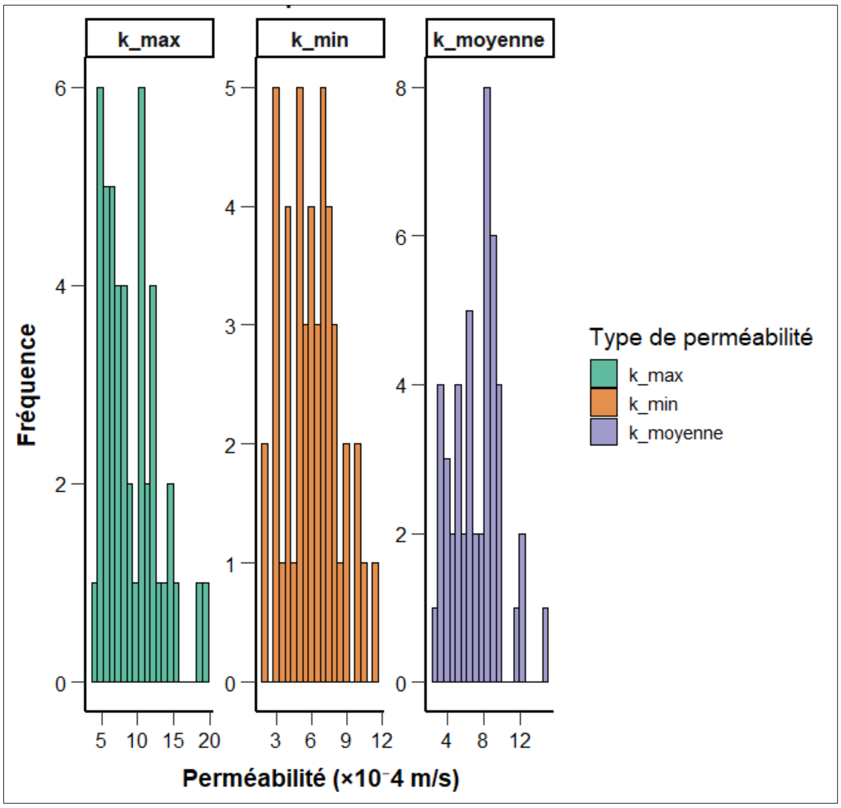

Figure 4 Distribution of induced permeabilities

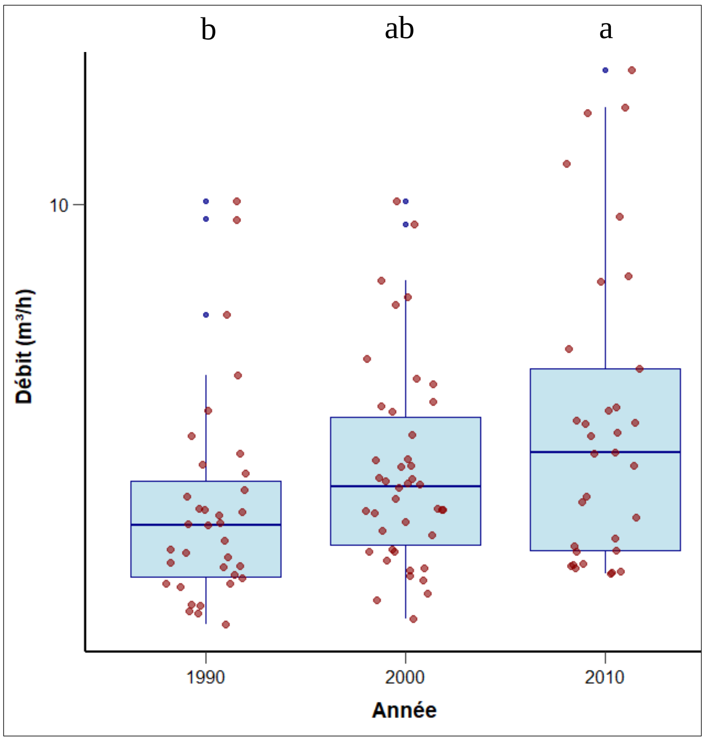

Figure 5 Evolution of operating flows (1990-2010)

4. Discussion

4.1. Structural control of aquifer productivity: convergences and divergences with conceptual models

The results obtained confirm a positive relationship between alteration thickness and drilling productivity up to 60 m, corroborating [7], in connection with the increase in the volume of storage in the altered zone. Above 60 m, the drop in flows contradicts the linear models of [19] and is explained by complex factors including the geometry and hydraulic properties of the altered zones, suggesting the existence of a critical threshold beyond which compaction and clogging limit productivity [1].

The hydraulic zonation, with a maximum productivity between 25 and 80 m, corresponds to the two-layer model of African basement aquifers validated by [20]. However, the early decrease in productivity from 80 m onwards could result from local lithological variations or from the intensity of regional tectonic processes [21].

4.2. Contribution of remote sensing: methodological validation and analytical limits

PCA is very effective for the identification of structural lineaments, concentrating 99.91% of the information in the first principal component, confirming the results [22]. However, the small contribution of the secondary components (CP2: 0.45%) contrasts with the 2-5% observed by [23], suggesting a more marked spectral homogeneity or different acquisition conditions.

The correlation between fracturing density and drainage network confirms the structural control of drainage in the crystalline domain [24]. However, this correlation remains less pronounced than in the Appalachians (r = 0.89, indicating the influence of local morphoclimatic factors and the contextual variability highlighted by [25].

4.3. Fracture-induced permeabilities: coherence and regional singularities

The induced permeabilities measured (1.13×10^{-2} to 1.97×10^{-4} m/s) are in the upper part of the known values for crystalline basement aquifers, exceeding those reported by [26] and approaching the exceptional cases documented by [27]. This performance probably reflects the intensity of regional fracturing, but exceeds the typical values for granitic formations (10^{-6} to 10^{-4} m/s, [28], raising questions about spatial representativeness or the influence of recent tectonic events.

The identification of four main NE-SW trending circulation corridors, atypical compared to classical dendritic or rectangular networks, suggests a regional structural control possibly related to major tectonic accidents and pan-African events [29]. However, the lack of deep geophysical data limits the validation of this hypothesis.

5. Conclusion

This research demonstrates the superiority of the multi-source approach for the analysis of fracturing in a West African crystalline context. The integration of satellite and aerial imagery reveals a network dominated by the N0-10° and N90-100° directions, consistent with the post-Pan-African stress field, and validates a robust length–number correlation model. The results confirm the hydraulic efficiency of the network between 1990 and 2010. The demonstration of a geometric-hydrodynamic correlation and the proposal of a transposable operational zonation make quantitative remote sensing, coupled with field validation, a powerful alternative to traditional geophysical methods for the optimization and security of the exploitation of basement aquifers.

Compliance with ethical standards

Disclosure of conflict of interest

No conflict of interest to be disclosed.

References

[1] Bianchi M., Palamakumbura R.N., MacDonald A.M., Macdonald D.M.J. Assessing regional variation in yield from weathered basement aquifers in West Africa and modelling their future groundwater development and sustainability. Hydro. J. 2023; 31: pp. 257-274

[2] Ani M., Jaunat J., Marin B., Huneau F., Gnandi K. Using archive hydrogeological data to enhance the hydrodynamic knowledge of hardrock aquifers in Western Africa. Journal of African Earth Sciences. 2025; 221: pp.105477.

[3] IPCC (2021): Climate Change 2021: The Physical Science Basis. Contribution of Working Group I to the Sixth Assessment Report of the Intergovernmental Panel on Climate Change [Masson-Delmotte, V., P. Zhai, A. Pirani, S.L. Connors, C. Péan, S. Berger, N. Caud, Y. Chen, L. Goldfarb, M.I. Gomis, M. Huang, K. Leitzell, E. Lonnoy, J.B.R. Matthews, T.K. Maycock, T. Waterfield, O. Yelekçi, R. Yu, and B. Zhou (eds.)]. Cambridge University Press, Cambridge, United Kingdom and New York, NY, USA, In press, doi:10.1017/9781009157896

[4] Boitt, M., Khayasi, P. and Wambua, C. Assessment of Groundwater Potential and Prediction of the Potential Trend up to 2042 Using GIS-Based Model and Remote Sensing Techniques for Kiambu County. International Journal of Geosciences. 202; 14: 1036-1063.

[5] Alshehri, F.; Mohamed, A. Analysis of Groundwater Storage Fluctuations Using GRACE and Remote Sensing Data in Wadi As-Sirhan, Northern Saudi Arabia. Water; 2023: 15, 282. https://doi.org/10.3390/w15020282

[6] Chander, G., Markham, B., and Helder, D. Summary of Current Radiometric Calibration Coefficients for Landsat MSS, TM, ETM+, and EO-1 ALI Sensors. Remote Sensing of the Environment. 2009; 113: 893-903.

[7] Dewandel B., P. Lachassagne, R. Wyns, J.C. Maréchal et N.S. Krishnamurthy (). A generalized 3-D geological and hydrogeological conceptual model of granite aquifers controlled by single or multiphase weathering. J. Hydrol. 2006 ; 330 : 260-284.

[8] Alle I. C., Descloitres M., Vouillamoz J. M., Yalo N., Lawson F. M. A., and Adihou A. C. Why 1D Electrical Resistivity Techniques Can Result in Inaccurate Siting of Boreholes in Hard Rock Aquifers and Why Electrical Resistivity Tomography Must Be Preferred: The Example of Benin, West Africa. J of African Earth Sc. 2018; 139: 341-353.

[9] Osseni A. A., Gbesso G. H. F., Akabassi, G. C., Akakpo B. A. Spatial Diagnosis and Conceptualisation of Greening Plan of Seme-Podji, Benin (West Africa). J of Environ. Geogra. 2023; 16: DOI: 10.14232/jengeo-2023-44431.

[10] Jourda J. P., Kouamé K. J, Saley M. B., Kouadio B.H et Oga Y.S. Contamination of the Abidjan aquifer by sewage: An assessment of extent and strategies for protection. In: Groundwater pollution in Africa (Edited by Yongxin X. and Brent U.). 2006; 291-300, Taylor and Francis/Balkema, Great-Britain.

[11] Mardia, K.V. and Jupp, P.E. Directional Statistics. 2000. John Wiley and Sons, London.

[12] Batayneh A., Ghrefat H., Diabat A. (2012). Journal of Earth Science. 2012, 23(6): 873-880. https://doi.org/10.1007/s12583-012-0298-6.

[13] Barton, N., Bandis, S. et Bakhtar, K. Strength, deformation and conductivity coupling of rock joints. int. J. Rock Mech. Min. Sci. and Geomech. Abstr. 1985 ; 22 : 121-140.

[14] Dershowitz, W.S. and Herda, H.H. (1992) Interpretation of Fracture Spacing and Intensity: Dershowitz, W S; Herda, H H Proc 33rd US Symposium on Rock Mechanics, Santa Fe, 3-5 June 1992 P757-766. Publ Rotterdam: A A Balkema, 1992. International Journal of Rock Mechanics and Mining Sciences and Geomechanics Abstracts, 30, A212. https://doi.org/10.1016/0148-9062(93)91769-f.

[15] Schuite J. 2013. Modelling of the transport properties of fractured peridotites from New Caledonia (South-West Pacific). Master's thesis, University of Montpellier 2, 53 p.

[16] Oda M. Permeability tensor for discontinuous rock masses. Géotechnique. 1985 35(4) : 483-495

[17] Laluet P. Estimation of agricultural water based on remote sensing: from irrigation to drainage. Hydrology. Paul Sabatier University - Toulouse III, 2023. 218 p.

[18] Van Buuren, S. et Groothuis-Oudshoorn, K. Mice: Multivariate imputation by chained equations in R. Journal of Statistical Software. 2011; 45(3): 1-67.

[19] Lachassagne, P., Wyns, R., Dewandel, B. The fracture permeability of hard rock aquifers is due neither to tectonics, nor to unloading, but to weathering processes. Terra Nova. 2011; 23: 145-161.

[20] Courtois N., Lachassagne P., Wyns R., Blanchin R., Bougaïré F.D., Somé S., Tapsoba A. Large-Scale Mapping of Hard-Rock Aquifer Properties Applied to Burkina Faso. Ground Water. 2010; 48: 269-283

[21] Maréchal JC, Dewandel B, Subrahmanyam K. Use of hydraulic tests at different scales to characterize fracture network properties in the weathered-fractured layer of a hard rock aquifer. Water Resources Research. 2004; 40 (11): 1-17

[22] Sander, R. and Crutzen. P. J. Model stud! indicating halogen activation and ozone destruction in polluted air masses transported to the sea. J. Geohys. Res. (Atmos.). 1996; 101: 9121-9138.

[23] Liu, J.G. and Mason, P.J. Essential Image Processing and GIS for Remote Sensing. UK : John Wiley and Sons Ltd ; 2009. 437p.

[24] Magowe M., Carr J.R. Relationship between lineament and ground water occurrence in western bostwana Ground Water, 1999; 37(2): 282-286.

[25] Oularé S., Kouamé K. F., Saley M. B., Aké G. E., Adja G. M., Kouamé K.A. and Therrien R. Estimation and validation of the depth of aquifers in the N'zo basin, Côte d'Ivoire, by the WTR model. Physio-Geo. 2025; 8(1): 1-25.

[26] Wright E.-P. The hydrogeology of crystalline basement aquifers in Africa. Hydrogeology of Crystalline Basement Aquifers in Africa. E. P. a. B. Wright, E.G., Geological Society Special Publication, London. 1992 ; 66 : 1-27.

[27] Leray S. Characterization of crystalline basement aquifers and their water resources - Contribution of "age" data of water. Applied geology. University of Rennes 1, 2012.

[28] Freeze, R.A. and Cherry, J.A. Groundwater. Prentice-Hall Inc., Englewood Cliffs. 1979; 7632: 604.

[29] Chorowicz, J., and Fabre, J. Organization of drainage networks from space imagery in the Tanezrouft plateau (Western Sahara): Implications for recent intracratonic deformations. Geomorphology. 1997. 21(2); 139-151.